Mecánica Computacional Vol. XXIV
A. Larreteguy (Editor)
Buenos Aires, Argentina, Noviembre 2005

A STRONG COUPLING SCHEME FOR FLUID-STRUCTURE INTERACTION PROBLEMS WITH DYNAMICALLY MOVING BOUNDARIES IN VISCOUS INCOMPRESSIBLE FLOWS

J. Yang[*], S. Preidikman[†], and E. Balaras[*]

[*] Department of Mechanical Engineering
University of Maryland at College Park
College Park, Maryland, 20742, USA
e-mail: jmyang@glue.umd.edu, balaras@eng.umd.edu

[†] Facultad de Ingeniería
Universidad Nacional de Río Cuarto
Ruta Nacional 36 Km 601, 5800 Río Cuarto, Argentina
e-mail: spreidik@vt.edu

Key words: Fluid Structure Instructions, Strong Coupling, Immersed Boundary Method, Incompressible Flows.

Abstract. *In the present paper an embedded-boundary formulation that is applicable to fluid structure interaction problems is presented. The Navier-Stokes equations for incompressible flow are solved on a fixed grid which is not aligned with the body. A corotational formulation is used to describe the dynamics of a body that moves through the fixed grid undergoing large-angle/large-displacement rigid body motions. A strong coupling scheme is adopted, where the fluid and the structure are treated as elements of a single dynamical system, and all of the governing equations are integrated simultaneously and interactively in the time-domain. A demonstration of the accuracy and efficiency of the method will be given for a variety of fluid/structure interaction problems.*

1 INTRODUCTION

Numerical simulations of fluid flows interacting with dynamically moving boundaries are amongst the most challenging problems in computational mechanics. The main difficulty comes from the fact that the spatial domain occupied by the fluid changes with time, and the location of the boundary is usually an unknown itself that depends on the fluid flow and the solution of additional equations describing the motion/deformation of the body. There is only a limited number special cases where established boundary-conforming formulations can be directly applied to such problems with a relatively small overhead. The use of moving reference frames[8], or coordinate transformations[11,16] are characteristic examples. In more complex configurations formulations utilizing moving and/or deforming grids that continously adapt to the changing location of the body have to be adopted (see for example [17, 15]). For problems that involve multiple bodies undergoing large motions and/or deformations, these algorithms are fairly complicated and have an adverse impact on the accuracy and efficiency of the fluid solvers.

Recently, non-boundary conforming formulations are increasingly gaining attention as tools to study fluid structure interaction problems (see [9] for a recent review). A common feature in these methods is the solution of the Eulerian form of the Navier-Stokes equations on a fixed grid, and tracking of the moving body in a Lagrangian fashion. Consequently, the grid lines and the surface of the body are almost never aligned. Their advantage compared to boundary-conforming formulations is that the need for regeneration and/or deformation of the grid is eliminated and in most cases efficient Cartesian solvers can be used. On the other hand, the imposition of boundary conditions on the moving body is not trivial, and a variety of strategies with different degrees of accuracy and complexity have been developed over the years. The 'immersed-boundary' formulation introduced by Peskin[14], for example, uses a smooth forcing function to enforce velocity boundary conditions on elastic bodies. The forcing function can be directly derived from some constitutive law applicable to the elastic body under consideration. To the limit of rigid bodies, however, such laws are not well posed and the derivation of the forcing field can be problematic. To overcome this limitation, alternative strategies like the 'embedded-boundary' method[4] have been developed. In this case a forcing function is also used to impose boundary conditions; it is not, however, specified in the continuous space by means of some physical arguments, but rather in the discrete space by directly requiring the solution to satisfy the boundary conditions. The approach can be fairly complex if the spatial discretization utilizes a large stencil, but it enforces boundary conditions with accuracy that is equivalent to that of boundary-conforming formulations.

Embedded-boundary formulations have been mainly used in simulations with stationary rigid bodies[4,7,18,2]. This is due to complications introduced to the temporal integration scheme by grid points that change phase (for example a point in the solid body can became a point in the fluid at the next timestep and vise-versa) as the boundary moves on the Eulerian grid. Recently Yang & Balaras[22] proposed field-extension strategy that addresses this issue. Results on two-dimensional laminar flows and three-dimensional turbulent flows interacting with complex boundaries undergoing prescribed motions were in excellent agreement with reference experiments and simulations. In the present study a formulation that extends this

method to problems where there is a two way interaction between the fluid and the body, whose motion will be now determined by structural properties and the fluid forces, will be presented. Emphasis will be given on the coupling scheme which is critical for the accuracy and efficiency of the overall method. In particular, we will present a strong coupling scheme, where the fluid and the structure are treated as elements of a single dynamical system, and all of the governing equations are integrated simultaneously and interactively in the time-domain. The details on the numerical method will be given in the next section. A validation of the method will be given in the results section, where vortex induced vibrations in circular cylinders with one and two-degrees of freedom are considered. Conclusions and future recommendations with be given in the final section.

2 PROBLEM FORMULATION AND NUMERICAL METHODS

The governing equations for unsteady incompressible viscous flow are:

$$\frac{\partial u_i}{\partial t} = -\frac{\partial u_i u_j}{\partial x_j} - \frac{\partial p}{\partial x_i} + \frac{1}{\mathrm{Re}} \frac{\partial^2 u_i}{\partial x_j \partial x_j} + f_i, \tag{1}$$

$$\frac{\partial u_i}{\partial x_i} = 0, \tag{2}$$

where $x_i \left(i = 1, 2, 3\right)$ are the Cartesian coordinates, u_i are the velocity components in the corresponding directions normalized by a reference velocity U, and p is the pressure normalized by ρU^2 with ρ the density of the fluid, and f_i represents a external body force field. The Reynolds number is defined as, $\mathrm{Re} = UL/\nu$, where is L a reference length scale and ν the kinematic viscosity of the fluid.

The equation of motion that is generally governing the motion of a two-dimensional, elastically mounted body, oscillating in the ($X-Y$) plane has the from:

$$\mathbf{M}\ddot{\mathbf{x}}(t) + \mathbf{C}\dot{\mathbf{x}}(t) + \mathbf{K}\mathbf{x}(t) = \mathbf{f}\left[\mathbf{x}(\tau), \dot{\mathbf{x}}(\tau), \ddot{\mathbf{x}}(\tau)\right], \quad \forall \tau \in 0 \le \tau \le t \tag{3}$$

where $\mathbf{M}$ is the mass matrix, $\mathbf{C}$ is the damping matrix, $\mathbf{K}$ is the stiffness matrix and $\mathbf{f}$ is the vector of generalized hydrodynamic forces per unit span, and $\mathbf{x}(t) = X_0(t)\mathbf{i} + Y_0(t)\mathbf{j} + \Theta(t)\mathbf{k}$ is the vector of generalized structural displacements. Here, $X_0(t)$ and $Y_0(t)$ are the displacements of the center of mass of the body in the x and y directions, respectively, and $\Theta(t)$ is the rotation around an axis perpendicular to the ($X-Y$) plane.

Equations (1) and (2) governing the dynamics of the fluid, and equation (3) governing the dynamics of the body need to be solved in a coupled manner. In the present study a strong coupling scheme is adopted, where the fluid and the structure are treated as elements of a single dynamical system, and all governing equations are integrated simultaneously in the time-domain. A fundamental complication with the application of a time-domain approach to two-way, fluid-structure interaction problems like the one described above, is that the prediction of the flow field and hydrodynamic loads

requires knowledge of the motion of the structure and vice-versa. To address this issue an iterative predictor-corrector scheme is adopted. It is based on Hamming's 4th-order, predictor-corrector method[3]. Hamming's scheme was adapted to the present problem to avoid evaluating the hydrodynamic loads at fractional time steps and to accommodate hydrodynamic loads that are proportional to the acceleration (the so called added-mass effect). In the following paragraphs the fluid flow solver, the structural solver and the coupling scheme will be discussed in detail.

2.1 Fluid flow solver

The governing equations (1) and (2) are solved using a highly efficient fractional step method on a staggered Cartesian grid. All spatial derivatives are approximated using second-order central differences. The time advancement scheme is a second-order Adams-Bashforth scheme, where all terms in the right-hand-side (RHS) of momentum equations are advanced explicitly. The overall splitting scheme can be summarized as follows:

$$\begin{aligned}\frac{\hat{u}_i^k - \hat{u}_i^{k-1}}{\Delta t} &= RHS_i^k + f_i^k \\ &= -\frac{3}{2}H\left(u_i^{k-1}\right) + \frac{1}{2}H\left(u_i^{k-2}\right) - \frac{\partial p^{k-1}}{\partial x_i} + f_i^k,\end{aligned} \tag{4}$$

$$\frac{\partial^2 \phi^k}{\partial x_i \partial x_j} = \frac{1}{\Delta t}\frac{\partial \hat{u}_i^k}{\partial x_i}, \tag{5}$$

$$u_i^k = \hat{u}_i^k - \Delta t \frac{\partial \phi^k}{\partial x_i}, \tag{6}$$

$$p^k = p^{k-1} + \phi^k \tag{7}$$

where k is the timestep index, $\hat{u}_i^k$ is the intermediate velocity, ϕ is the pressure correction, H is a spatial operator containing the convective and viscous terms, f_i^k is the discrete forcing function used to impose boundary conditions on an arbitrary immersed boundary that does not coincide with the underlying grid and Δt is the time step.

An immersed body moving on the fixed Cartesian grid is tracked in a Lagrangian manner using a series of marker particles. After establishing the grid-interface relation, all Cartesian grid nodes are split into the three categories shown in Fig. 1a.: (1): *fluid-points*, which are points in the fluid phase; (2) *forcing points*, which are grid points in the fluid phase with one or more neighboring points in the solid phase; (3) *solid-points*, which are points in the solid phase. The details on the tracking scheme and tagging procedure can be found in [2]. The Navier-Stokes solver described in the previous paragraph is applied on all points of the Eulerian grid as if the fluid/solid interface is not present. The effect a moving solid body on the flow is introduced through the discrete forcing function, f_i. It is computed only at the

forcing points by substituting $\hat{u}_i^k$ with u_Ψ in equation (4) and solving for f_i:

$$f_i^k = \frac{u_\Psi - u_i^{k-1}}{\Delta t} - RHS_i^k, \tag{8}$$

In the special case where the interface and the forcing point coincide, u_Ψ is simply the local velocity on the rigid body, and therefore the boundary condition one wishes to enforce. In the general case, however, the points on the Eulerian grid and the interface almost never coincide and u_Ψ has to be computed using some interpolation strategy. An example is shown in Fig. 1b, where the velocity at the forcing point is computed by means of linear interpolation that involves the projection of the forcing point on the interface (point 1 in Fig. 1b) and two points in the fluid phase (points 2 and 3 in Fig. 1b). In the general case the velocity or any variable, , in the two-dimensional space can be written as follows:

$$\phi = b_1 + b_2 x + b_3 y \tag{9}$$

The coefficients b_1, b_2, and b_3 in Eq. (9) can be found by solving the following system:

$$\begin{Bmatrix} b_1 \\ b_2 \\ b_3 \end{Bmatrix} = \mathbf{A}^{-1} \begin{Bmatrix} \phi_1 \\ \phi_2 \\ \phi_3 \end{Bmatrix} = \begin{bmatrix} 1 & x_1 & y_1 \\ 1 & x_2 & y_2 \\ 1 & x_3 & y_3 \end{bmatrix}^{-1} \begin{Bmatrix} \phi_1 \\ \phi_2 \\ \phi_3 \end{Bmatrix} \tag{10}$$

where (x_1, y_1), (x_2, y_2), and (x_3, y_3) in the 3×3 matrix $\mathbf{A}$ are the coordinates of the three points in the interpolation stencil shown in Fig. 1b. The inversion of matrix, $\mathbf{A}$, at every forcing point is performed every time the location of the interface is updated. Higher-order reconstructions for both Dirichlet and Newmann boundary conditions can be achieved in a straightforward manner using the same overall procedure (see for example [18]). The above solver has been extensively tested for a variety of laminar and turbulent flow problems involving stationary and moving immersed boundaries with prescribed motion with results in excellent agreement with reference computations and experiments[2,22].

2.2 ODE Solver and strong coupling scheme

Equation (3) can be rewritten in non-dimensional form, as a system of $2n$ first-order, non-linear, ordinary-differential equations (n is the number of degrees-of-freedom of the structure) as follows:

$$\dot{\mathbf{y}}(t) = \mathbf{F}\left[\mathbf{y}(\tau), \dot{\mathbf{y}}(\tau)\right], \quad \forall \tau \in 0 \le \tau \le t, \tag{11}$$

where half of the vector $\mathbf{F}$ represents generalized velocities and the other half represents generalized forces divided by the corresponding inertias. In general the loads depend explicitly on $\mathbf{y}$, and implicitly on the history of the motion and the acceleration of the structure. Hamming's 4th-order, predictor-corrector method is used to integrate equation (11)

in the time domain[3]. The details of the basic numerical procedure used to determine the current value of the vector $\mathbf{y}$ are given next:

1. Let $t_j = j\Delta t$ denote the time at the j-th time step, where Δt is the time-step size used to obtain the numerical solution, and
$$\mathbf{y}^j = \mathbf{y}\left(t_j\right), \quad \dot{\mathbf{y}}^j = \dot{\mathbf{y}}\left(t_j\right), \quad \mathbf{F}^j = \mathbf{F}\left[\mathbf{y}\left(t_j\right), \dot{\mathbf{y}}\left(t_j\right)\right] \tag{12}$$
2. Compute the predicted solution, ${}^p\mathbf{y}^j$, and modify it, ${}^1\mathbf{y}^j$, using the local truncation error, $\mathbf{e}^{j-1}$, from the previous time step:
$${}^p\mathbf{y}^j = \mathbf{y}^{j-1} + \frac{4}{3}\Delta t\left(2\mathbf{F}^{j-1} - \mathbf{F}^{j-2} + 2\mathbf{F}^{j-3}\right), \quad {}^1\mathbf{y}^j = {}^p\mathbf{y}^j + \frac{112}{9}\mathbf{e}^{j-1} \tag{13}$$
3. Correct the modified, predicted solution by:
$${}^{k+1}\mathbf{y}^j = \frac{1}{8}\left[9\mathbf{y}^{j-1} - \mathbf{y}^{j-3} + 3\Delta t\left({}^k\mathbf{F}^j + \mathbf{F}^{j-1} - \mathbf{F}^{j-2}\right)\right] \tag{14}$$

where ${}^k\mathbf{F}^j = \mathbf{F}\left({}^k\mathbf{y}^j\right)$ and ${}^1\mathbf{y}^j = {}^p\mathbf{y}^j$. k is the iteration index. Convergence is achieved when the iteration error, $e^j = \left\| {}^{k+1}\mathbf{y}^j - {}^k\mathbf{y}^j \right\|_\infty$ is less than a prescribed tolerance ε.

4. Compute the local truncation error, $\mathbf{e}^j$, and the final solution, $\mathbf{y}^j$, at step j and advance to the next timestep:
$$\mathbf{e}^j = \frac{9}{121}\left({}^{k+1}\mathbf{y}^j - {}^p\mathbf{y}^j\right), \quad \mathbf{y}^j = {}^{k+1}\mathbf{y}^j - \mathbf{e}^j \tag{15}$$

Note that in the above procedure information from four previous timesteps is required. Therefore, starting from the initial conditions, Euler, Adams-Moulton, and Adams-Bashforth methods were used.

The fluid solver described in Section 2.1 is coupled to the structural solver as follows:

1. Find the predicted location and velocity of the body using equation (13).
2. Find the predicted fluid velocity and pressure fields using equations (4)-(7) with the boundary conditions provided by step 1. Then, compute the resulting loads on the structure.
3. Compute the new location and velocity of the body using equation (14).
4. Check for convergence. If e^j is greater than the prescribed tolerance, ε, repeat steps 2 to 4. If convergence is achieved goto step 5.
5. Find final position and velocity of the body using equation (15), and the final fluid pressure and velocity fields from equations (4)-(7).

In all computations reported in this study a tolerance of $\varepsilon = 10^{-8}$ was used. The number of iterations required for convergence at each time step varied from 2 to 6 depending from the stiffness of the problem.

3 RESULTS

Vortex-induced vibrations of circular cylinders is a problem that has been extensively studied both experimentally and numerically (see [20] for a recent review), and will be used in the present study to evaluate the accuracy and efficiency of the proposed methodology. Initially two different configurations of a single cylinder are considered: 1. free oscillations in the cross-stream direction (one degree-of-freedom); 2. free oscillations in both the streamwise and cross-stream directions (two degrees-of-freedom). For both cases the selected parametric space is as close as possible to well documented laminar two-dimensional flow problems in the literature. Finally to demonstrate the efficiency and robustness of the proposed approach, test problems involving and array of freely oscillating cylinders are presented.

3.1 Free vertical oscillations

For a cylinder freely oscillating in the cross-stream direction, Y, which is modeled as mass-damper-spring system, the non dimensional form of equation (3) becomes :

$$\ddot{y} + 2\zeta\left(\frac{2\pi}{U_{red}}\right)\dot{y} + \left(\frac{2\pi}{U_{red}}\right)^2 y = \frac{1}{2n}C_L, \tag{16}$$

where $y = Y_0/D$ is the non-dimensionalized vertical displacement, $\zeta = c/2\sqrt{km}$ is the viscous damping ratio, $C_L = f_y/\left(\frac{1}{2}\rho DLU_\infty^2\right)$ is the lift force coefficient, $n = m/\rho D^2$ is the mass ratio with ρ the fluid density, and $U_{red} = U_\infty/f_n D$ is the reduced velocity with $f_n = \frac{1}{2\pi}\sqrt{k/m}$ the natural vibrating frequency of the structure. In the above m is system mass, c the damping coefficient, k the spring constant, Y_0 the transverse displacement of the system centroid, and f_y the instantaneous lift force on cylinder. Note that the same reference scales as in the Navier-Stokes equations (the cylinder diameter, D, and the freestream velocity, U_∞) were used to obtain the dimensionless form of the equations.

The parametric space was selected to match the experiment by Anagnostopoulos and Bearman[1], which has been used for validation in several other numerical simulations (see for example [12,19,15,8]). The mass ratio was set to $n = 117.10$ and damping ratio to $\zeta = 0.0012$. A sketch of the computational domain is given in Fig. 2a. The inflow boundary is located $10D$ upstream of the cylinder where a uniform velocity is specified. At the outflow boundary, located $30D$ downstream of the cylinder, a convective boundary conditions is used[13]. Radiative boundary conditions are used in both the freestream boundaries. The

number of grid points in all computations was 320×240 in streamwise and transverse directions, respectively. The grid was stretched in both directions and the resulting resolution near the cylinder was approximately $0.02D \times 0.02D$. A detail of the grid is shown in Fig. 2b. A constant time step of $0.005D/U_\infty$ was used for all cases.

For all cases the flow over a stationary cylinder for the same Reynolds number was initially computed. Then, the cylinder was allowed to move freely. Integration in time was performed until a periodic state of constant maximum amplitude was reached. The large mass ratio of this system makes the problem fairly stiff and very long integration times were necessary in all cases. In the lock-in regime and for the low Reynolds number, one can observe a monotonically growing oscillation amplitude (see Fig. 3a). Approximately 2500 non-dimensional time units were necessary for a periodic state to be achieved. As the Reynolds number increases in the lock-in regime the amplitude stops to increase monotonically (see Fig. 3b). Over time, however, it also approaches a periodic state of lower maximum amplitude. Outside the lock-in regime there is a drastic change in the vibration amplitude which is modulated and has a very small magnitude as shown in Fig. 3c for $Re = 90$. In this case the cylinder oscillation frequency is $f_c = 0.165$, which is very close to vortex shedding frequency of the fixed cylinder at this Reynolds number.

The maximum oscillation amplitude and the corresponding frequency is shown in Fig. 4 as a function of the Reynolds number. The experimental results in [1] and previous computations [12,19,15,8] have been added for comparison. All reference computations have been conducted using boundary conforming formulations. In particular, Nomura[12] and Wei et al.[19] used and arbitrary Lagrangian Eulerian (ALE) finite element formulation, where the computational grid is deformed/regenerated every time the location of the cylinder changes to conform to the body at all times. A similar strategy was used by Schulz and Kallideris[15] in the framework of a finite-volume formulation. Li et al.[8] used a highly accurate spectral element method with a translating frame of reference to avoid the tedious process of grid regeneration. As shown in Fig. 4a all simulations agree on the critical Reynolds number for lock-in, which is however, lower compared to the one reported in the experiment. The corresponding values are approximately $Re \sim 90$ in the simulations and $Re \sim 103$ in the experiment. Schulz and Kallinderis[15] speculated that this difference could be due three-dimensional effects induced by the absence of end-plates in the experimental apparatus.

In all different data sets the maximum vibration amplitude in the lock-in regime appears at the lowest Reynolds number as shown in Fig. 4b. Discrepancies, however, can be observed regarding actual values of the amplitude, A/D. In general, all simulations tend to under-predict the values of A/D reported in the experiment. Our results are in good agreement with the highly accurate spectral element computations reported in [8]. *An extensive grid refinement study, however, remains to be performed to establish the grid independency of our solutions*. The vorticity and pressure contours for the case of maximum amplitude in the lock-

in regime ($Re = 95$) is shown in Fig. 5. The smoothness of the pressure and vorticity fields near the cylinder are indicative of the accuracy of the proposed formulation. Also, the expected $2S$ mode pattern (two single vortices per cycle of motion) can be seen in the wake, which is in agreement with the observations in [21].

3.2 Free oscillations in the *X*-*Y* plane

Although in many practical problems cylindrical structures have the same mass ratio and natural frequency in both the *X* and *Y* directions, far fewer studies have been conducted with the cylinder oscillating in the *X*-*Y* plane. This is partially due to the fact that early experiments did not show significantly different response characteristics compared to cylinders undergoing oscillations in the vertical direction only. Recently, however, Jauvtis and Williamson[6] in their water channel experiments at Reynolds numbers ranging from 1,000 to 15,000, reported a new response branch that involves substantial oscillation amplitudes in the streamwise direction when the mass ratio is very low ($n \sim 2.5$). In the laminar flow regime, which is the focus of the present work, such a dramatic change in the response of the system would be probably absent as indicated by a the few two-dimensional numerical simulations at low Reynolds numbers (see for example [10], [23]). To further investigate this issue and also establish the efficiency and accuracy of the proposed formulation we conducted a number of numerical experiments of freely oscillating cylinders in the *X*-*Y* plane at a fairly wide parametric space. We kept the Reynolds number, mass ratio, and dumping ratio - $Re = 200$, $n = 2.04$ and $\zeta = 0.00425$ respectively- constant, and varied the reduced velocity, U_{red}, from 1 to 11. This way we covered approximately the same range as in the experiments in [6], at a much lower Reynolds number.

The computational box and boundary condition set-up is similar to the one used for the vertically oscillating cylinder. The grid has been modified, however, to ensure appropriate resolution in a wider range. The number of grid points in all computations was 400×360 in streamwise and transverse directions respectively, resulting in near cylinder resolution of approximately $0.02D \times 0.02D$ (same as the one-degree-of-freedom case above). As for the previous case, in all computations the corresponding stationary cylinder problem was first solved and then free vibrations in both directions were allowed. Due to the low mass ratio in this case, a stable periodic state was achieved much faster compared to the previous problem.

Figure 6 shows the oscillation frequency, transverse oscillation amplitude, and the streamwise oscillation amplitude as function of the reduced velocity. A lock-in regime ranging from approximately $4 < U_{red} < 6$ is evident. In this regime the transverse oscillation amplitude is fairly high, but always below the 0.6 limit for laminar flows discussed in [20]. The streamwise amplitude is lower by a factor of 10 in agreement with previous computations. Also, the oscillation frequencies are approximately equal to the natural oscillation frequency of the structure. On the same figure we added the corresponding results from the one-degree-of-freedom case reported in the previous section. Qualitatively the response of the two

systems is similar. The one-degree-of-freedom case, however, has narrower lock-in range with a lower maximum amplitude, which is probably due to the higher mass ratio and differences in the Reynolds numbers.

The *X*, *Y* trajectories of the cylinder center for the case with the largest amplitude ($U_{red} = 4.1$) are shown in Fig. 7a. Both trajectories are approximately sinusoidal leading to the well known figure-eight type of motion shown in Fig. 7b. The corresponding force coefficients on the other hand, deviate from the sinusoidal variation resulting in the complex pattern shown in Fig. 8. This is a result of the streamwise motion and is similar to corresponding plots reported in [6]. Finally, in Fig. 9 isolines of the vorticity and pressure are shown at one instant during the cycle for the case of $U_{red} = 4.1$. The $2S$ vortex pattern is evident.

4 SUMMARY

In the present paper an embedded-boundary formulation that is applicable to fluid structure interaction problems is presented. The Navier-Stokes equations for incompressible flow are solved on a fixed grid and the body is tracked in a Lagrangian reference frame. A strong coupling scheme is presented, where the fluid and the structure are treated as elements of a single dynamical system, and all of the governing equations are integrated simultaneously, and interactively in the time-domain. Results presented for cases of vortex induced vibrations in a circular cylinder were in good agreement with reference data in the literature.

5 REFERENCES

[1] Anagnostopoulos, P., and Bearman, P. W., "Response characteristics of a vortex-excited cylinder at low Reynolds numbers", *J. Fluids Struct.*, **6**, 39-50, (1992)

[2] Balaras, E., "Modeling complex boundaries using an external force field on fixed Cartesian grids in large-eddy simulations", *Computers & Fluids*, **33**, 375-404, (2004).

[3] Carnahan, B., Luther, and H. A., Wilkes, J.O., *Applied Numerical Methods*, John Wiley & Sons, Inc., New York, (1969).

[4] Fadlun, E. A., Verzicco, R., Orlandi, P., and Mohd-Yusof, J., "Combined immersed-boundary finite-difference methods for three-dimensional complex flow simulations", *J. Comput. Phys.*, **161**, 35-60, (2000).

[5] Hu, H. H., Patankar, N. A., and Zhu, M. Y., "Direct numerical simulations of fluid-solid systems using the arbitrary Lagrangian-Eulerian Technique", *J. Comput. Phys.*, **169**, 427-462, (2001).

[6] Jauvtis, N., and Williamson, C. H. K., "The effect of two degrees of freedom on vortex-induced vibration at low mass and damping", *J. Fluid Mech*, **509**, 23-62, (2004).

[7] Kim, J., Kim, D., and Choi, H., "An immersed-boundary finite-volume method for simulations of flow in complex geometries", *J. Comput. Phys.*, **171**, 132-150, (2001).

[8] Li, L., Sherwin, S. J., and Bearman, P. W., "A moving frame of reference algorithm for fluid/structure interaction of rotating and translating bodies", *Int. J. Numer. Meth. Fluids*, **38**, 187-206, (2002).

[9] Mittal, R., and Iaccarino, G., "Immersed boundary methods", *Annu. Rev. Fluid Mech.*, **37**, 239-261, (2005).
[10] Newman, D. J., and Karniadakis, G. E., "Direct numerical simulations of flow over a flexible cable", In Proc. *6th Int. Conf. Flow-Induced Vibrations*, ed. P. W. Bearman, Rotterdam, Netherlands, 193-203, (1995).
[11] Newman, D. J., and Karniadakis, G. E., "A direct numerical simulation study of flow past a freely vibrating cable", *J. Fluid Mech.*, **344**, 95-136, (1997).
[12] Nomura, T., "Finite element analysis of vortex-induced vibrations of bluff cylinders", *J. Wind Eng. Ind. Aerodyn.*, **46-47**, 595-604, (1993).
[13] Orlanski, I., "Simple boundary-condition for unbounded hyperbolic flows", *J. Comput. Phys.*, **21**, 251-269, (1976).
[14] Peskin, C. S., "Flow patterns around heart valves: a numerical method", *J. Comput. Phys.*, **10**, 252-271, (1972).
[15] Schulz, K. W., and Kallinderis, Y., "Unsteady flow structure interaction for incompressible flows using deformable hybrid grids", *J. Comput. Phys.*, **143**, 569-597, (1998).
[16] Shen, L., Zhang, X., Yue, D. K. P., and Triantafyllou, M. S., "Turbulent flow over a flexible wall undergoing a streamwise traveling wave motion", *J. Fluid Mech.*, **484**, 197-221, (2003).
[17] Tezduyar, T. E., "Finite Element methods for flow problems with moving boundaries and interfaces", *Archives of Computational Methods in Engineering*, **8**, 83-130, (2001).
[18] Tseng, Y. H., and Ferziger, J. H., "A ghost-cell immersed boundary method for flow in complex geometry", *J. Comput. Phys.*, **192**, 593-623, (2003).
[19] Wei, R., Sekine, and A., Shimura, M., "Numerical analysis of 2D vortex-induced oscillations of a circular cylinder", *Int. J. Numer. Meth. Fluids*, **21**, 993-1005, (1995).
[20] Williamson, C. H. K., and Govardhan, R., "Vortex-induced vibrations", *Annu. Rev. Fluid Mech.*, **36**, 413-455, (2004).
[21] Williamson, C. H. K., and Roshko, A., "Vortex formation in the wake of an oscillating cylinder", *J. Fluids Struct.*, **2**, 355-381, (1988).
[22] Yang, J., and Balaras, E., "An embedded-boundary formulation for large-eddy simulation of turbulent flows interacting with moving boundaries", *J. Comput. Phys.*, Submitted for Publication, (2005).
[23] Zhou, C. Y., So, R. M. C., and Lam, K., "Vortex-induced vibrations of an elastic circular cylinder", *J. Fluids Struct.*, **13**, 165-189, (1999).

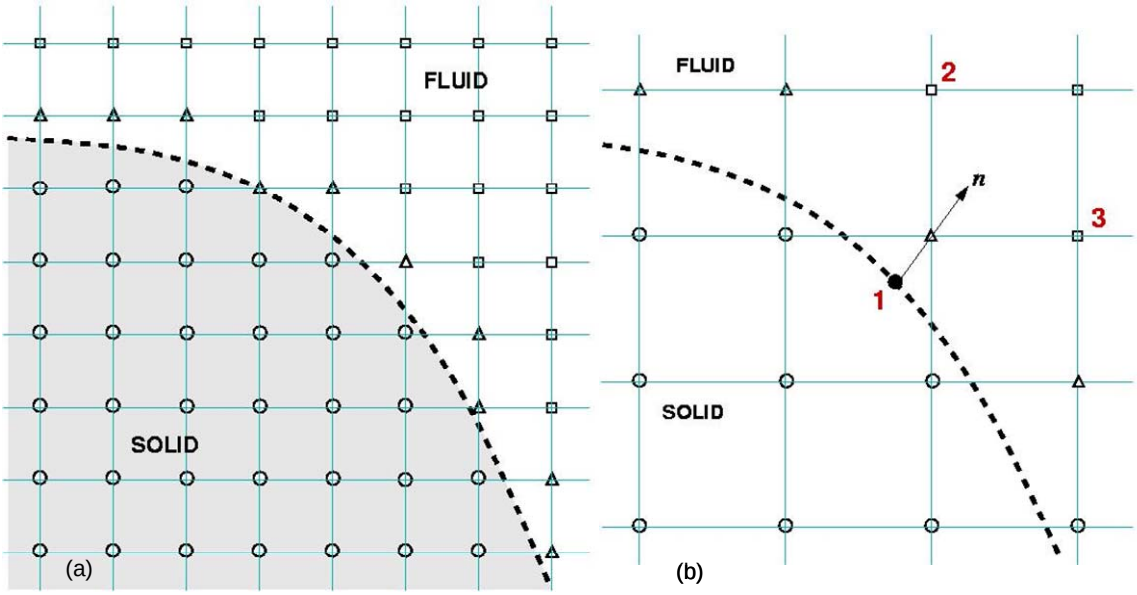

Figure 1: (a) Tagging of grid nodes on the Eulerian grid according to their location relative to the fluid/solid interface indicated by the dashed line; ○ solid points; □ fluid points; △ forcing points. (b) Example of a linear local reconstruction stencil involving the projection of the forcing point to the interface (point 1) and two fluid points (points 2 and 3).

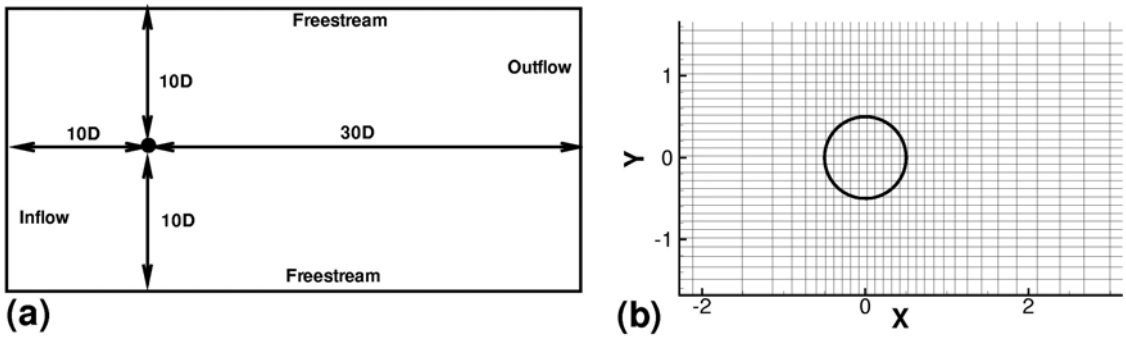

Figure 2: Problem set-up for the free vibrating cylinder in the cross-stream direction. (a) Sketch of the computational domain; (b) close-up of grid near the cylinder (every five points are shown).

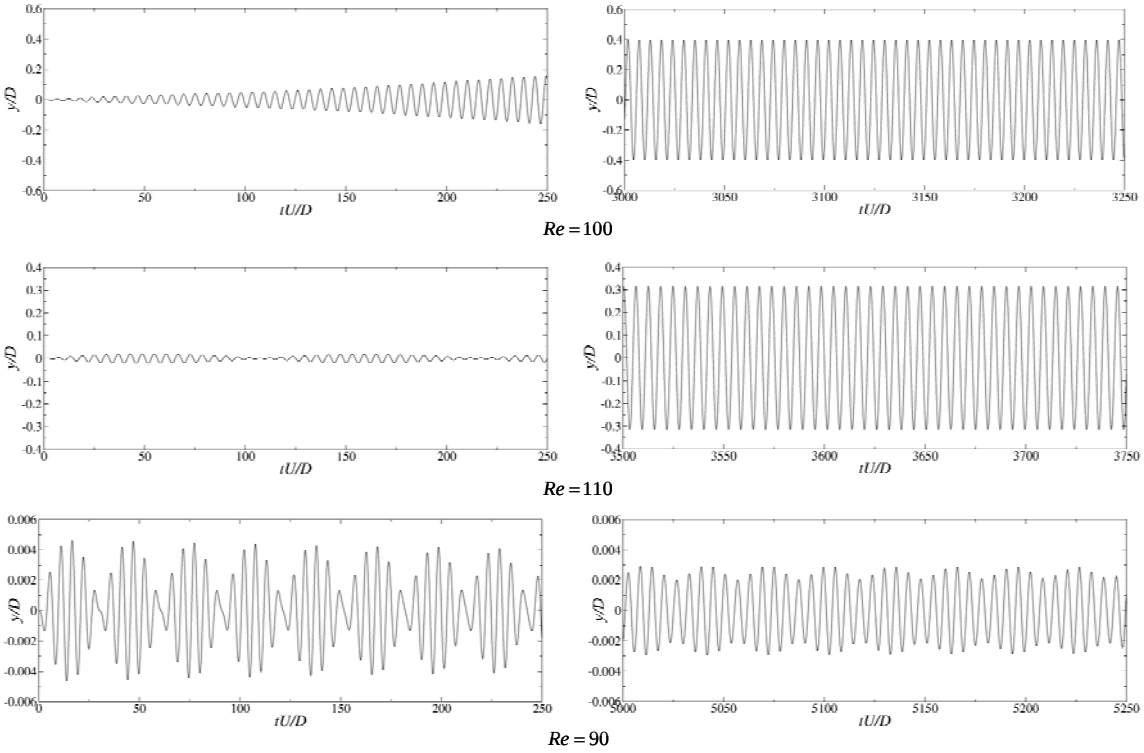

Figure 3: Time history of the displacements for the freely vibrating cylinder in the cross-stream direction. (a) and (b) are Reynolds number in the lock-in regime; (c) is outside the lock-in regime.

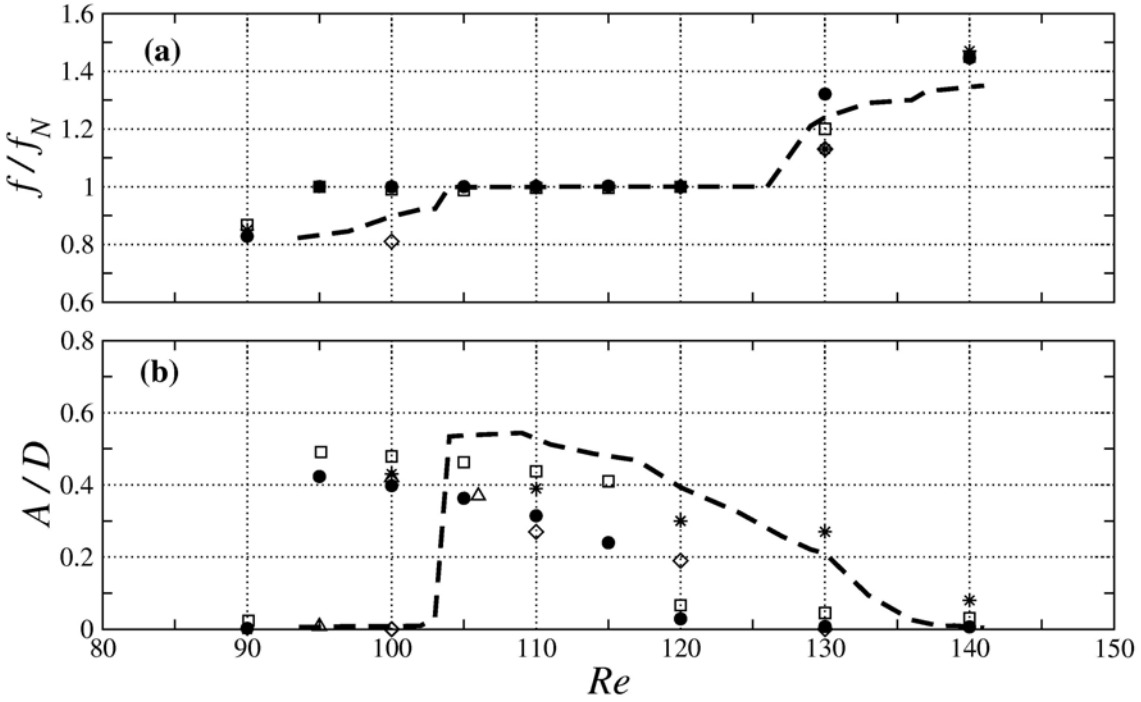

Figure 4: Comparison of: (a) frequency of the oscillation f/f_n ; (b) maximum oscillation amplitude A/D, as a function of the Re number. • present computations; --- experiment in [1]; ◊ computation in [12]; * computation in [19]; □ computation in [15]; ∆ computation in [8].

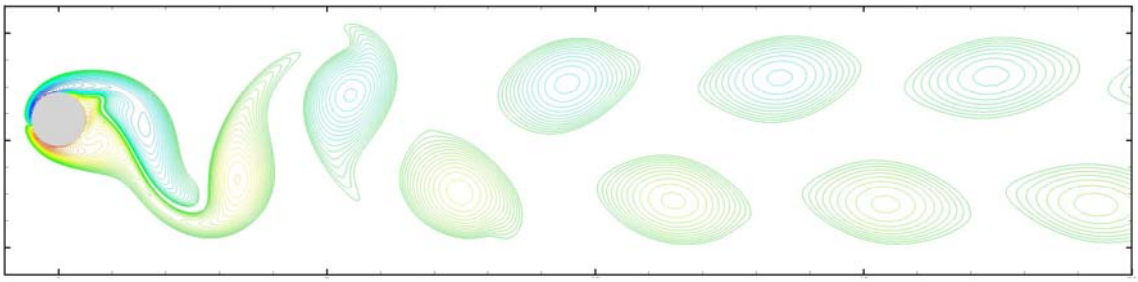

(a) Vorticity

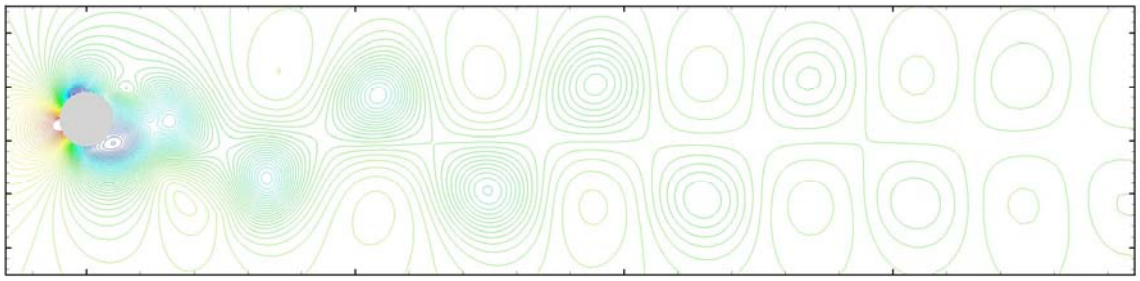

(b) Pressure

Figure 5: Freely vibrating cylinder in the cross-stream direction.
(a) Spanwise vorticity isolines; (b) pressure isolines $Re = 95$, $U_{red} = 5.29$.

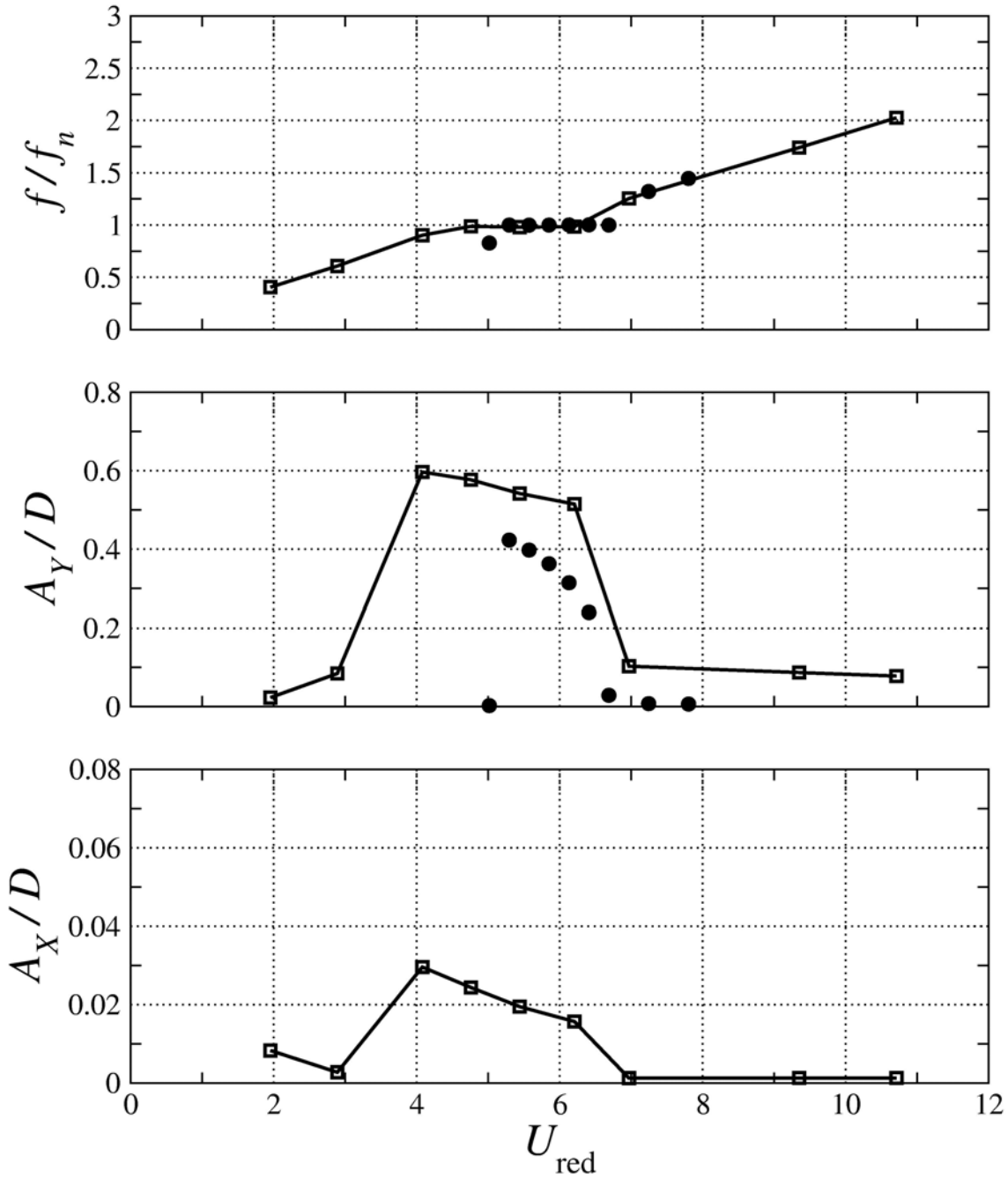

Figure 6: The oscillation frequency, transverse oscillation amplitude and streamwise oscillation amplitude as functions of reduced velocity. □ two-degrees-of-freedom; • one-degree-of-freedom.

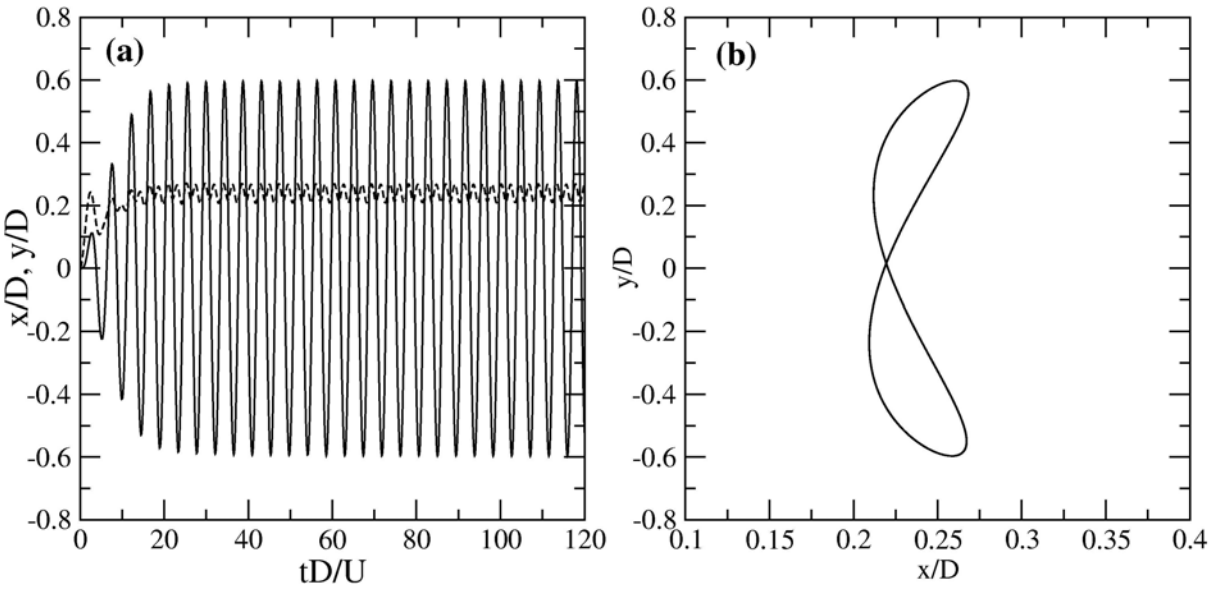

Figure 7: Freely vibrating cylinder in the ($X-Y$) plane during lock-in. (a) Time history of the displacements, — x-direction and --- y-direction; (b) final, periodic displacement pattern. $Re = 200$, $U_{red} = 4.1$.

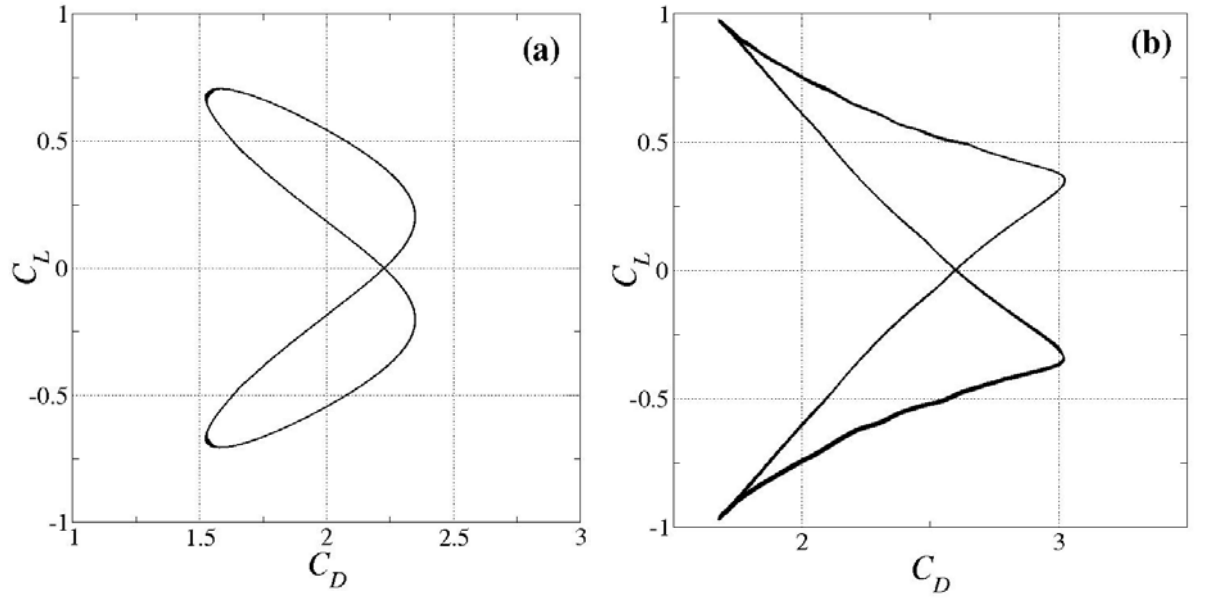

Figure 8: Phase plots for the lift and drag coefficients. (a) One-degree-of-freedom, $Re = 95$, $U_{red} = 5.1$; Two-degrees-of-freedom, $Re = 200$, $U_{red} = 4.1$.

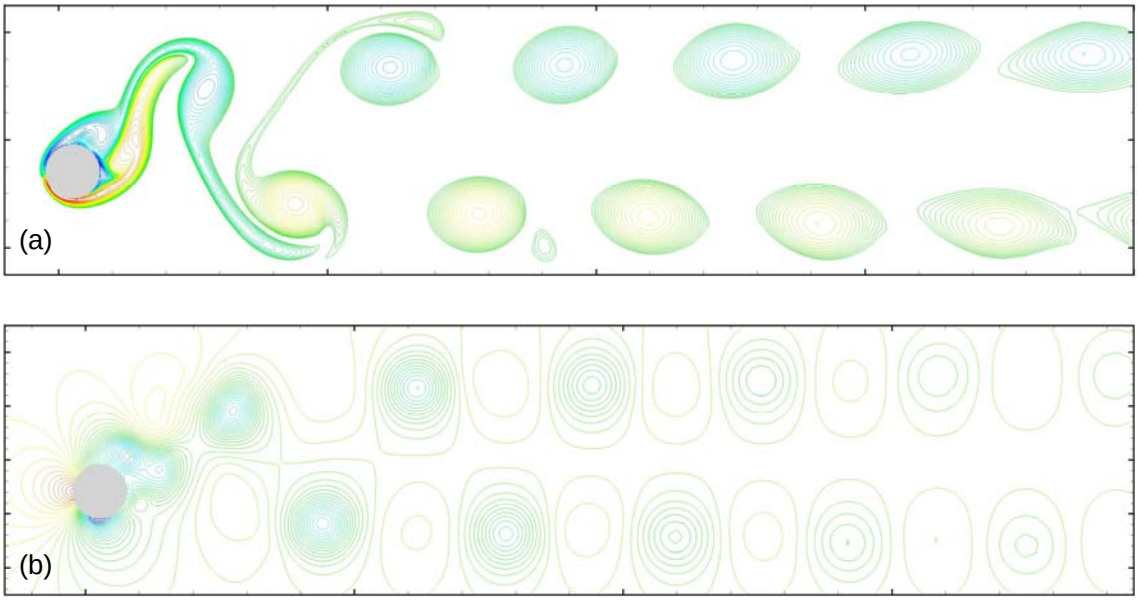

Figure 9: Freely vibrating cylinder in the $X-Y$ plane. (a) Spanwise vorticity isolines; (b) pressure isolines. $Re = 200$, $U_{red} = 4.08$.